

Portland State University

**PDXScholar**

---

Mechanical and Materials Engineering Faculty  
Publications and Presentations

Mechanical and Materials Engineering

---

8-2022

# A Lacunarity-Based Index for Spatial Heterogeneity

Ryan H. Scott

*Portland State University, rhs2@pdx.edu*

Hawwa Falih Kadum

*Portland State University, hawwa@pdx.edu*

G. Salmaso

*University of Utah*

Marc Calaf

*University of Utah*

Raul Bayoan Cal

*Portland State University, rcal@pdx.edu*

Follow this and additional works at: [https://pdxscholar.library.pdx.edu/mengin\\_fac](https://pdxscholar.library.pdx.edu/mengin_fac)



Part of the [Mechanical Engineering Commons](#)

**Let us know how access to this document benefits you.**

---

## Citation Details

Scott, R., Kadum, H., Salmaso, G., Calaf, M., & Cal, R. B. (2021). A Lacunarity Based Index for Spatial Heterogeneity. *Earth and Space Science*, e2021EA002180.

This Article is brought to you for free and open access. It has been accepted for inclusion in Mechanical and Materials Engineering Faculty Publications and Presentations by an authorized administrator of PDXScholar. Please contact us if we can make this document more accessible: [pdxscholar@pdx.edu](mailto:pdxscholar@pdx.edu).



## RESEARCH ARTICLE

10.1029/2021EA002180

## A Lacunarity-Based Index for Spatial Heterogeneity

R. Scott<sup>1</sup> , H. Kadum<sup>1</sup> , G. Salmaso<sup>2</sup> , M. Calaf<sup>2</sup> , and R. B. Cal<sup>1</sup><sup>1</sup>Mechanical and Materials Engineering, Portland State University, Portland, OR, USA, <sup>2</sup>Mechanical Engineering, University of Utah, Salt Lake City, UT, USA

## Key Points:

- A general spatial heterogeneity measure is proposed for one, two, and three dimensional data
- Maximum heterogeneity scales and index values are reported for known systems
- Our approach is applied to fractured sea ice images and compares favorably to existing measures

## Correspondence to:

R. Scott and R. B. Cal,  
rhs2@pdx.edu;  
rcal@pdx.edu

## Citation:

Scott, R., Kadum, H., Salmaso, G., Calaf, M., & Cal, R. B. (2022). A lacunarity-based index for spatial heterogeneity. *Earth and Space Science*, 9, e2021EA002180. <https://doi.org/10.1029/2021EA002180>

Received 13 DEC 2021

Accepted 8 JUN 2022

## Author Contributions:

**Conceptualization:** R. Scott, H. Kadum**Data curation:** R. Scott**Formal analysis:** R. Scott, R. B. Cal**Funding acquisition:** M. Calaf, R. B. Cal**Investigation:** R. Scott, H. Kadum, G. Salmaso**Methodology:** R. Scott, H. Kadum, G. Salmaso**Project Administration:** M. Calaf, R. B. Cal**Supervision:** M. Calaf, R. B. Cal**Validation:** R. Scott, H. Kadum, G. Salmaso**Visualization:** R. Scott**Writing – original draft:** R. Scott**Writing – review & editing:** R. Scott, H. Kadum, M. Calaf, R. B. Cal

© 2022 The Authors. Earth and Space Science published by Wiley Periodicals LLC on behalf of American Geophysical Union.

This is an open access article under the terms of the [Creative Commons Attribution-NonCommercial-NoDerivs License](https://creativecommons.org/licenses/by/4.0/), which permits use and distribution in any medium, provided the original work is properly cited, the use is non-commercial and no modifications or adaptations are made.

**Abstract** Characterizing spatial heterogeneity is fundamental in numerous areas, yet defining spatial patterns often depends on qualitative assessments or a priori knowledge. Lacunarity analysis is a popular occupancy-based method for identifying relevant length scales in spatially heterogeneous systems. From lacunarity, we identify the existence of a point which encapsulates the spatial heterogeneity of a given system. This value satisfies the conditions for the lacunarity cutoff function and forms the basis of a heterogeneity index. We evaluate the behavior of both parameters in monofractal, clustered, and periodic systems. In addition, we demonstrate the broad utility of our approach to the scientific community by classifying the spatial heterogeneity of fractured sea ice and comparing our findings to existing measures. The heterogeneity index produced a linear correlation with the area fraction of open ocean to ice with an  $R^2$  of 0.967.

**Plain Language Summary** Random patterns in nature are challenging to quantify yet have a profound impact on the behavior of Earth systems. We propose a new index to identify when a pattern is no longer random and an index to rank how random it is compared to a uniform proxy. We demonstrate the response of both measures to known patterns and use these parameters to describe the characteristics of fractured sea ice. We also compare our index to existing measures to determine the effectiveness of our method.

## 1. Introduction

Random or semirandom patterns are prevalent in natural systems yet quantifying the spatial heterogeneity of such geometries is challenging. Lacunarity has been shown to reveal characteristic length scales in complex systems (Kirkpatrick & Weishampel, 2005) with applications in diverse topics including landscape ecology (Andronache et al., 2016; Frazer et al., 2005; Malhi & Román-Cuesta, 2008; Plotnick et al., 1993; Saunders et al., 2005; With & King, 1999), earth sciences (Liu & Ostadhassan, 2017; Williams, 2015; Xia et al., 2019; Zeng et al., 1996), and medicine (Borys et al., 2008; Dougherty & Henebry, 2001; Gould et al., 2011; Hadjileontiadis, 2009; Popovic et al., 2018; Yasar & Akgunlu, 2005). Lacunarity outperforms fractal dimension and compares favorably to the multifractal spectra leading to complementary analyses where both lacunarity and multifractal spectra are employed (Gould et al., 2011; Kirkpatrick & Weishampel, 2005; Popovic et al., 2018; Saunders et al., 2005; Yasar & Akgunlu, 2005; Zeng et al., 1996). Mandelbrot (1982) introduced the concept of lacunarity as a measure of the space filling nature of fractal geometries. Allain and Cloitre (1991) expanded on the concept of lacunarity through the gliding box algorithm which has since formed the foundation of lacunarity analysis. The gliding box algorithm is a counting technique applicable to both binary and quantitative data sets (Plotnick et al., 1996). Their approach was initially described in one dimension but extends to higher dimensional spaces where a square of side length  $r$  is used in two dimensions and a cube of side length  $r$  in three dimensions (Allain & Cloitre, 1991; Plotnick et al., 1996). In the gliding box algorithm, boxes of size  $r$  are iteratively translated across a system such that the entire domain is covered. At each location, the mean and variance of the mass density of elements occupying a box are determined and a lacunarity value calculated following Plotnick et al. (1996):

$$\Lambda(r) = \frac{\sigma^2(r)}{\mu(r)^2} + 1 \quad (1)$$

The lacunarity of a single box is insufficient to describe the spatial heterogeneity of an entire system thus values must be obtained for a range of box sizes (Allain & Cloitre, 1991). Calculating a sufficient number of boxes is computationally demanding so recent efforts have focused on developing optimized algorithms with remarkable reductions in execution time (Backes, 2013; Reiss et al., 2016; Tolle et al., 2008; Williams, 2015). We also report a fast implementation of the gliding box algorithm in Appendix A.

Interpreting lacunarity curves provides valuable insight into the nature of a complex system. In lacunarity analysis, values are computed for an arbitrarily large set of boxes then normalized by the smallest scale of lacunarity,  $\Lambda_1$ , and plotted on log-log axis. The slope of the resulting lacunarity curve is a measure of self-similarity while local minima indicate relevant length scales. However, relating these features to spatial structures in the base system requires qualitative assessment. Furthermore, it is not apparent from lacunarity curves alone whether one system is more heterogeneous than another. For instance, two monofractal systems may have similar fractal dimensions but manifest distinct patterns. Plotnick et al. (1996) examined this dynamic in regular, fractal, and clumped systems. They found domains with equivalent masses exhibit an even spread of average mass across scales while variance and thus lacunarity is directly related to the distribution of mass within a given system. Evenly dispersed systems produced low lacunarity values across scales but concentrated distributions lead to heightened variance and higher lacunarity values.

In order to facilitate quantitative rather than qualitative comparisons between systems, several single value representations of lacunarity curves have been suggested. Yet capturing their behavior with a single value is complex. Lacunarity indices have been proposed based on the characteristics of specific systems (Du & Yeo, 2002), while other metrics use features of the curve itself such as linear regions denoting self-similarity in the case of the  $\lambda$  scaling parameter (Allain & Cloitre, 1991), and the index of translational homogeneity (Malhi & Román-Cuesta, 2008). A more general approach is the average lacunarity given by Sengupta and Vinoy (2006) for a discrete system

$$\bar{\Lambda} = \ln \left( \frac{1}{N} \sum_{i=1}^N \Lambda(r_i) \right) \quad (2)$$

where  $N$  is the total number of boxes. While this approach derives a single value from a lacunarity curve, it does not include a cutoff function as prescribed by Allain and Cloitre (1991) leaving the maximum box size,  $r_{\max}$ , undefined. Because the total number of boxes and the maximum box size must be decided arbitrarily,  $\bar{\Lambda}$  is limited to distinguishing between systems with identical domains and box sizes.

Here, two developments are presented in Section 2.1 to produce a single heterogeneity index and address shortcomings present in current approaches. Data processing techniques are described in Section 2.2. Results for known patterns follow in Section 3.1 with an application to geophysical systems in Section 3.2. Concluding remarks and suggestions for implementation are presented in Section 4.

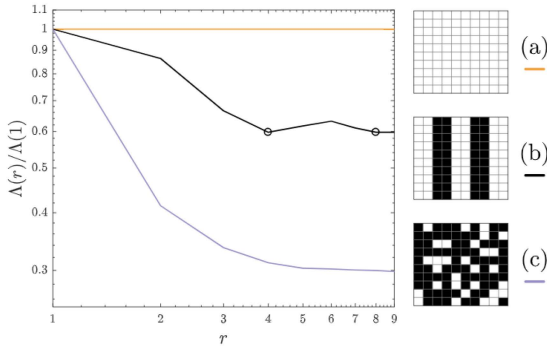
## 2. Methods

### 2.1. Definition of the Cutoff Function and Heterogeneity Index

The first development is the definition of the cutoff function necessary to determine the maximum box size. As  $r$  becomes large,  $\Lambda(r)$  decreases since larger boxes include more mass which eventually outweighs variance between boxes. At some scale,  $\Lambda(r_a)$  reaches a constant value of  $\Lambda(r \geq r_a) \approx 1$ . Because scales beyond  $r_a$  appear homogeneous, spatial heterogeneity is encapsulated within  $r_a$ . The cutoff function is then defined as the first box which satisfies  $\Lambda(r_a) \approx 1$  and  $d\Lambda(r_a)/dr \ll 1$ . Alternatively, if  $r$  reaches the domain size,  $\Lambda(r_d) = 1$  since all observable data are included in one box and the variance of a single observation is 0. In this case,  $r$  is set to the domain size since  $\Lambda(r_d)$  is dominated by sample size rather than system characteristics. With regard to lacunarity, a finite domain reduces variance in box mass such that the large-scale behavior of the system is shaped by sample size as described by Serafino et al. (2021). This implies either the system parameters or domain size are insufficient to capture the spatial heterogeneity of the full system. Sampling at sufficient resolution is impractical for many applications so care must be taken such that  $\Lambda(r_d) < \Lambda(1)$  to allow a meaningful comparison between scales. Additionally, normalizing each domain such that  $r_d/r_d \leq 1$  is needed to compare between systems with different domain extents and desirable in general to ensure  $r_a$  is a global rather than local point of reference.

The second development is the introduction of a heterogeneity index,  $h$ , which represents the information contained within a lacunarity curve as a single number. In order to reduce a curve to one value, we define the weighted average box size,  $\bar{R}_w$ , as

$$\bar{R}_w = \frac{1}{N_{\max}} \sum_{i=1}^{N_{\max}} \frac{r_i \Lambda(r_i)}{\Lambda(1)} \quad (3)$$



**Figure 1.** Sample domains with lacunarity curves for (a) homogeneous (b) heterogeneous, organized, and (c) heterogeneous, disorganized systems. In each image, white squares are occupied data with a value of 1 and black squares are vacancies with a value of 0. The initial cutoff point  $r_a = 4$  and its periodic repetition at  $r_a = 8$  are circled for the heterogeneous, organized system.

where  $N_{\max}$  is the number of boxes until either  $r_a$  or  $r_d$  is reached, denoted  $r_{\max}$ . We normalize  $\Lambda(r_i)$  by  $\Lambda(1) = 1$ . Although this quantity has units of length, the relationship between  $\bar{R}_w$  and the physical system is not immediately apparent. Additionally, a large range of values may be realized depending on system characteristics. As such,  $\bar{R}_w$  alone is insufficient to facilitate quantitative comparisons between systems. We instead seek an index in the range  $[0, 1]$  which can be found by first considering the homogeneous case for  $\bar{R}_w$ . In a homogeneous system,  $\Lambda(r) = 1$  since the variance in box masses is zero for all scales. In this case, Equation 3 reduces to the mean box size given by  $(1 + r_{\max})/2$  assuming box sizes increase by a fixed amount per iteration. An equivalent homogeneous system can then be defined as  $\bar{R}_H = (1 + r_{\max})/2$ . Subtracting Equation 3 from  $\bar{R}_H$  and rearranging leads to the heterogeneity index

$$h = 1 - \frac{2\bar{R}_w}{1 + r_{\max}} \quad (4)$$

By comparing  $\bar{R}_w$  to a homogeneous equivalent, our measure quantifies heterogeneity as the deviation in lacunarity at a given scale from the homogeneous case. Information from the full range of heterogeneous scales is included in

the measure by incorporating values through  $r_{\max}$ . Small values of  $h$  indicate a near-homogeneous system as  $\bar{R}_w$  approaches  $(1 + r_{\max})/2$ . Large values signify heterogeneity across a range of scales with substantial differences between  $\Lambda(1)$  and  $\Lambda(r_{\max})$ . A homogeneous system produces a value of  $h = 0$  while extreme heterogeneity yields  $h = 1$ . In the example presented in Figure 1, the homogeneous system produces  $\Lambda(r) = 1$  for all  $r$  and an index value of  $h = 0$  while the heterogeneous, disorganized system reaches  $r_d$  with an index value of  $h = 0.68$ . The heterogeneous, organized system falls between the two extremes with  $h = 0.29$ . Additionally, this system demonstrates a clear, repeated cutoff point equal to multiples of the row spacing,  $r_a = 4$ , due to its periodic nature.

## 2.2. Implementation and Data Processing

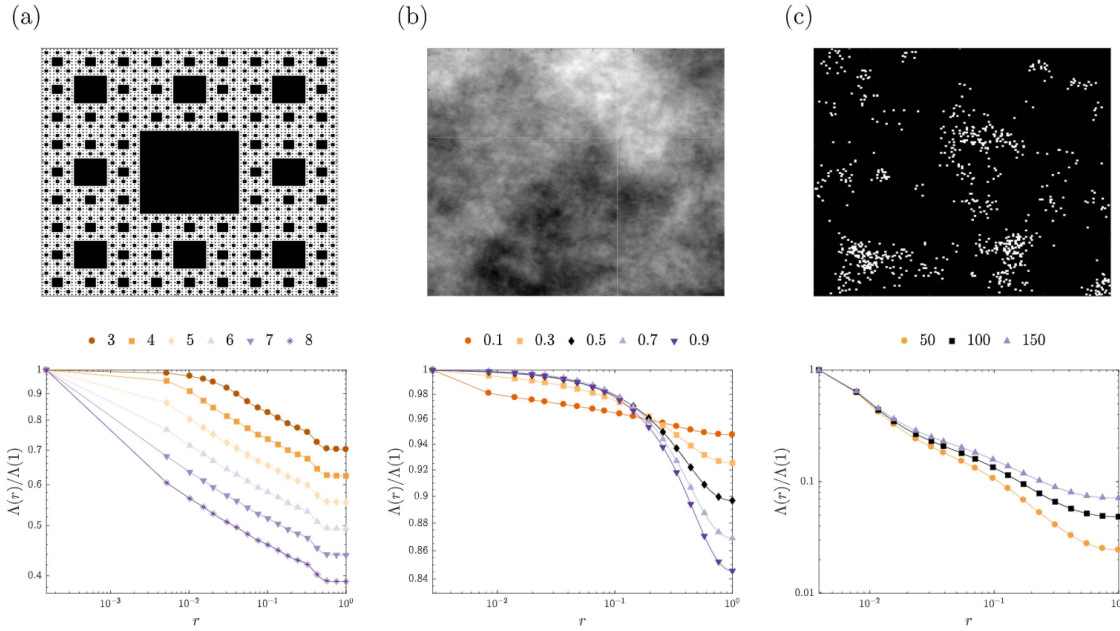
All data were processed in MATLAB 2018a on the Coeus HPC cluster at Portland State University. Each case was assigned one core on an Intel Xeon E2630 v4 processor with 20 GB of assigned RAM. Known systems were generated at runtime using algorithms by Kroese and Botev (2015). In all cases, the cutoff point,  $r_a$ , was selected as the first value with  $d\Lambda(r_a)/dr \leq 10^{-5}$  and  $\Lambda(r_a) = 1 \times 10^{-5}$  or set to the domain size  $r_d$ .

## 3. Results

### 3.1. Parameter Response to Defined Systems

Results are presented for monofractal, clustered, and periodic data representative of spatially heterogeneous problems from a variety of disciplines. Each system was selected to test the measures in response to specific physical features and represented on a unit domain  $D$ . Because clustered and fractional Brownian monofractal data rely on random number generation, 1,000 realizations were analyzed for each system to ensure reported quantities reflect overall system geometry rather than single instances. For these systems,  $r_a$  and  $h$  are reported as mean quantities with standard deviations.

A monofractal system is considered through six Sierpiński carpet (Sierpiński, 1916) generations with depths of 3, 4, 5, 6, 7, and 8. Spatial heterogeneity within the Sierpiński carpet is directly related to fractal depth where increasing depths recursively generate smaller features. As expected of monofractal systems, the lacunarity curve is linear until box sizes approach the cutoff point. A constant  $r_a$  is observed at  $r_a = 0.67D$  for all fractal depths. This value is the smallest box containing one complete subset of the Sierpiński carpet and the central vacancy visible in Figure 2a. The influence of small-scale heterogeneity is revealed through the heterogeneity index with sequentially increasing values of 0.71, 0.74, 0.77, 0.79, 0.82, and 0.84. As fractal depth increases, the presence of additional fine features lead to increased variance at small scales which in turn produces higher index values.



**Figure 2.** Single realizations of each system with normalized lacunarity curves. In order: (a) monofractal Sierpiński carpet with a fractal depth of 5 and normalized lacunarity curves for depths of 3, 4, 5, 6, 7, and 8. (b) Monofractal fractional Brownian field (FBF) with a Hurst parameter of 0.5 and normalized lacunarity curves for Hurst parameters of 0.1, 0.3, 0.5, 0.7, and 0.9. (c) Poisson process point clusters for  $\lambda = 50$  with normalized lacunarity curves for  $\lambda = 50, 100,$  and  $150$ . White squares are occupied with a value of 1, black squares are vacancies with a value of 0, and grayscale is used to represent intermediate values between (0, 1).

This behavior is also visible in Figure 2a where increasing fractal depth leads to greater differences between  $\Lambda(1)$  and  $\Lambda(r_a)$ .

Next we consider a monofractal system composed of five fractional Brownian fields (FBF; Kroese & Botev, 2015) with Hurst parameters,  $H$ , of 0.1, 0.3, 0.5, 0.7, and 0.9 shown in Figure 2b. FBF systems are continuously varying where the extent of spatial patterns within the domain depends on the Hurst parameter. Small Hurst parameters produce rough systems with many small features while large values result in a single smooth feature. In the method developed by Kroese and Botev (2015), the Hurst parameter is embedded in a circulant matrix to generate a quarter disk domain with consistent monofractal behavior at all scales. We selected a random square domain within each quarter disk to remove the influence of disk shape from lacunarity analysis. With 1,000 realizations,  $H = 0.1$  generated  $r_a = 0.9 \pm 0.1D$  for 99% of its iterations. At  $H = 0.3$ , the cutoff point grew to  $r_a = 0.96 \pm 0.08D$  with 74% of iterations producing suitable values. By  $H = 0.5$ , the cutoff point was indistinguishable from the domain size at  $r_a = 0.99 \pm 0.08D$  and only 41% of iterations satisfied the cutoff function. The proportion of iterations with suitable cutoff values decreased to 22% for  $H = 0.7$  and finally 9% for  $H = 0.9$ . Only  $H = 0.1$  generated a linear lacunarity curve as anticipated from a monofractal system. Because each domain is a subset of the quarter disk field, scales larger than the sampling window are interrupted. As the Hurst parameter increases, a larger proportion of scales are disrupted by the sampling window. Because only a portion of scales are available in the lacunarity analysis, the resulting curves do not display the expected behavior. Furthermore, the lack of cutoff points for FBF systems indicate these systems are driven by sample size. In all cases, the heterogeneity index is computed with  $r_d$  yielding values of 0.17, 0.09, 0.08, 0.06, 0.03. Because the FBF algorithm generates smoothly varying fields, variance between scales is low which in turn produces small index values. As the Hurst parameter increases, fewer fine features are present within the domain and the system approaches homogeneity as evidenced by low index values. Despite the limitations imposed by sample size, the index values are able to distinguish the relative roughness of FBF fields and identify low Hurst parameter fields as more heterogeneous.

Point clusters were generated through a two-dimensional Poisson process (Kroese & Botev, 2015) with initial point densities of  $\lambda = 50, 100,$  and  $150$  as shown in Figure 2c. All point densities produced  $r_a = 0.84 \pm 0.13D$

with 96% of iterations developing satisfactory cutoff values. Although point density increases between cases, location within the domain is governed by the Poisson process resulting in similar cutoff values. At a low density ( $\lambda = 50$ ) clusters are overdispersed and small relative to domain size. Index assignments reflect high spatial heterogeneity with  $h = 0.98$ . At a higher density ( $\lambda = 100$ ) voids between clusters are reduced making the system less heterogeneous with  $h = 0.97$ . Further increasing point density ( $\lambda = 150$ ) causes clusters to merge for the least heterogeneous index value of  $h = 0.96$ . It is worth noting the index values for each case are extremely high since variance is sensitive to data with a large portion of empty values. If identical patterns were created by removing points from a uniform domain, cutoff points would remain the same but the index values would be close to zero since the majority of points would be occupied.

### 3.2. Application to Geophysical Systems

Further insights are gained through the application of our approach to quantify the spatial heterogeneity of sea ice. This system is of particular relevance as sea ice develops fractures and melt pools across a large range of scales. Previous studies on sea ice have documented increased heat absorption in fragmented floes and variation in the atmospheric boundary layer in response to fracture size (Andreas, 1980; Andreas et al., 1979; Drüe & Heinemann, 2001; Shaw et al., 1991; Tetzlaff et al., 2015). Furthermore, because the albedo of sea ice is ~15 times the albedo of the surrounding ocean (Allison et al., 1993; Payne, 1972; Perovich & Polashenski, 2012), its heat absorption and climate impact are directly related to ice structure.

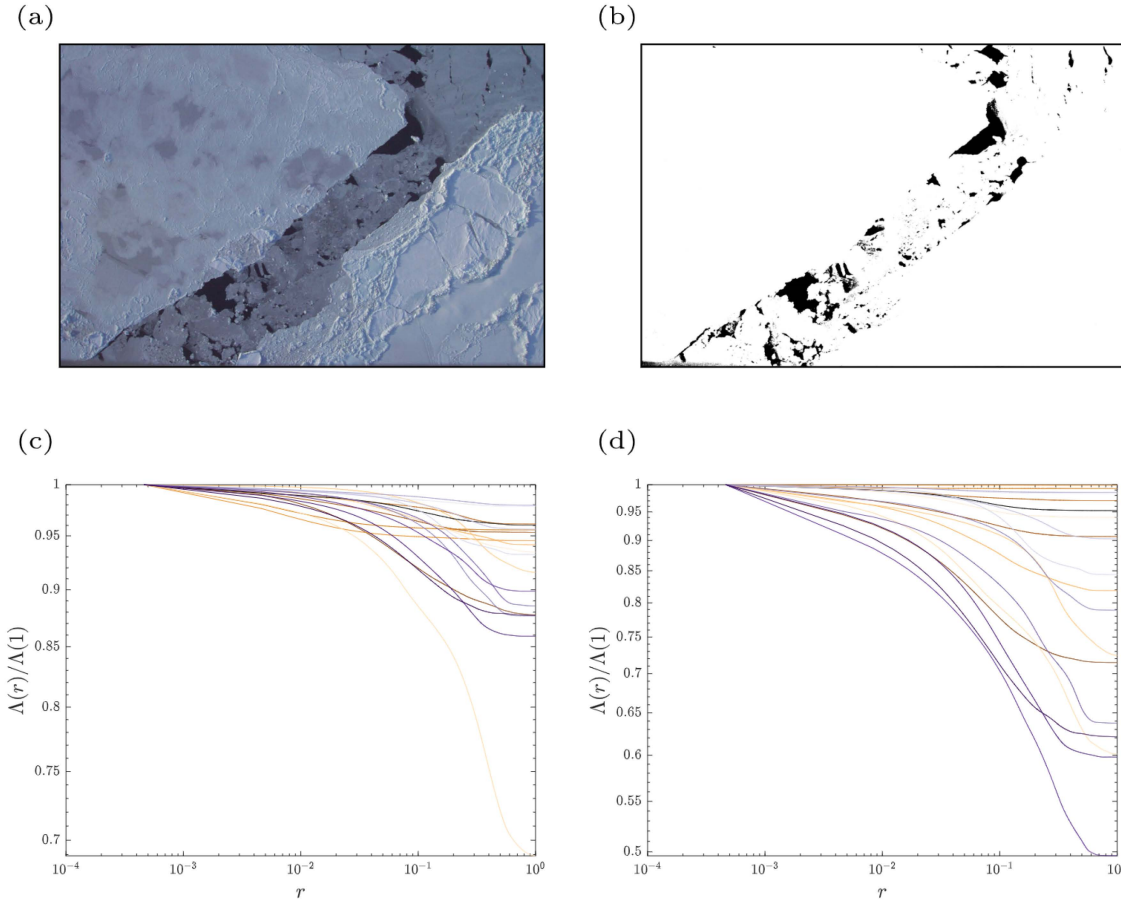
Arctic sea ice images were selected from the AMSRice06 aerial photograph database (Krabill, 2006). This database contains images from the Chukchi and Beaufort Seas of the Arctic Ocean depicting an assortment of sea ice structures in March 2006. Sample images were selected to cover the range of possible ice structures including uniform ice, open ocean, and fracture networks of varying scales. A simple ratio of ocean to ice pixels is used as a proxy for albedo as a complete study on deriving albedo estimates from aerial ice photographs is beyond the scope of the present work. Binary ice occupancy images were created by applying a 15% composite color difference threshold to raw color images in GNU Image Manipulation Program 2.8.22. Exposed water from open ocean, melt pools, and fracture networks were considered vacancies with a value of 0 while ice and snow cover were considered occupied and set to 1. Pixel designations were verified by hand for each image and additional artifacts such as aircraft landing gear were removed. Color images were converted to grayscale and normalized from 0 to 1. The normalization was performed across all images to provide global maximum and minimum values for comparison. In total, 19 images were selected and processed. An example is shown in Figure 3 and a table containing thumbnails of the complete image set along with their corresponding cutoff points and index assignments is provided in Appendix C.

Lacunarity curves for the chosen images are presented in Figure 3 for both grayscale and binary ice occupancy images. Grayscale images are sensitive to areas of open ocean with ice-ocean interfaces producing large variations in lacunarity across scales. Binary occupancy images respond to both continuous ice sheets and open ocean. Because the small differences in value from visible shadows and transparent ice are not present in the occupancy images, these systems appear homogeneous resulting in uniform lacunarity curves. In a similar manner, treating open ocean as voids leads to greater variation in lacunarity across scales. In all cases, a suitable value of  $r_a$  was identified within the domain and heterogeneity index values were assigned.

Correlations between the heterogeneity index and existing measures are presented in Figure 4. The  $q$ -statistic proposed by Wang et al. (2016) and spatial diversity index,  $H_s$ , developed by Claramunt (2005) are included to assess if the proposed metric,  $h$ , contributes additional useful information with regard to spatial heterogeneity. The  $q$ -statistic is designed to quantify spatial heterogeneity among user defined strata, in this case between ice and voids, and is expressed as

$$q = 1 - \frac{\sum_{h=1}^L \sum_{i=1}^{N_h} (Y_{hi} - \bar{Y}_h)^2}{\sum_{i=1}^N (Y_i - \bar{Y})^2} \quad (5)$$

where the study area is composed of  $N$  units and  $h = 1 \dots L$  stratum with each stratum containing of  $N_h$  units.  $Y_i$  and  $Y_{hi}$  denote the value of the  $i$ th in each sample. This measure is similar to lacunarity in that both quantify



**Figure 3.** Aerial sea ice images from AMSRice06 (Krabill, 2006) depicting fracture networks, melt pools, and open ocean with lacunarity curves. From left to right: (a) raw color image, (b) binary ice occupancy image, (c) lacunarity curves for all color images, and (d) lacunarity curves for all occupancy images. In (b), vacancies are black regions with a value of 0 and ice occupancy is represented with white regions with a value of 1. Image borders were added for presentation and are not included in analysis.

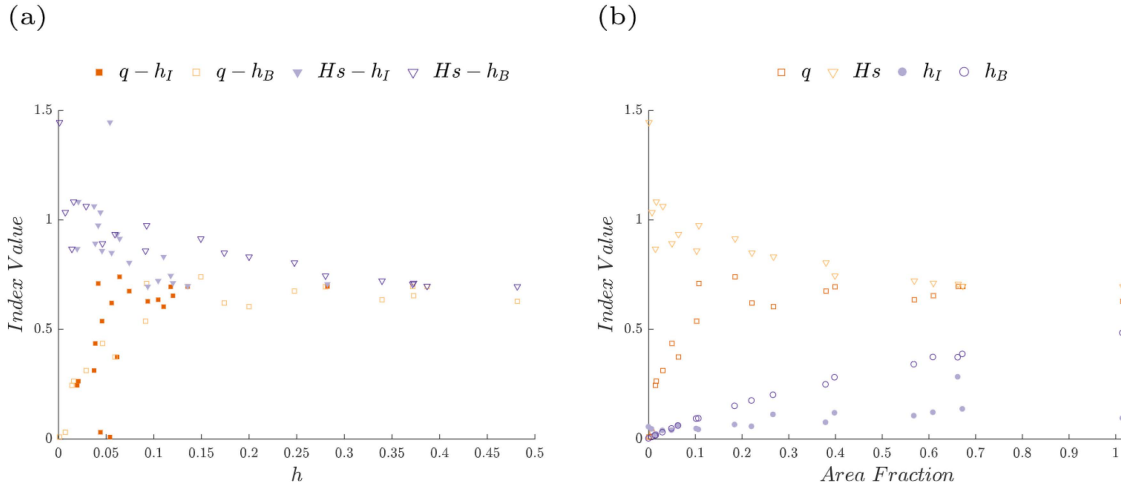
heterogeneity through variance at different locations. The primary difference is strata are user defined in the  $q$ -statistic whereas the lacunarity algorithm automatically partitions data into boxes. Following the procedure outlined by Wang et al. (2016), strata were defined from ice occupancy images and the  $q$ -statistic calculated from corresponding grayscale images.

The index of spatial diversity,  $H_s$ , considers heterogeneity through differences between the intradistance of entities in a given class and the extradistance of entities from all other classes as

$$H_s = - \sum_{i=1}^n \frac{d_i^{int}}{d_i^{ext}} p_i \log_2(p_i) \quad (6)$$

where  $n$  is the number of classes,  $d_i^{int}$  is the mean distance between members of class  $i$ ,  $d_i^{ext}$  is the mean distance between members of all other classes, and  $p_i$  is the proportion of data contained by class  $i$ . Because this measure is based solely on classification and distance, values were obtained from occupancy images.

In order to determine if  $h$  is a functional transform of an existing measure, the correlations in Figure 4a are considered. All correlations produced significant  $p$ -values of  $p \leq 0.05$ . However, the  $R^2$  fits were poor with values



**Figure 4.** Heterogeneity correlations between (a)  $q$ -statistic and  $Hs$  with the proposed index,  $h$ , and (b) all measures with ice occupancy area fractions, used as a simple Albedo surrogate. In (b),  $h_I$  increases for small area fractions then declines as ice distribution declines while  $h_B$  shows a near linear, increasing relationship with the Albedo surrogate across a wide range of ice fractions. Subscripts denote input data with  $I$  for grayscale images and  $B$  binary occupancy images.

of 0.0256 for  $q$  with  $h$  from grayscale images, 0.0531 for  $q$  with  $h$  from occupancy images, 0.293 for  $Hs$  with  $h$  from grayscale images, and 0.619 for  $Hs$  with  $h$  from occupancy images. Both  $q$  and  $Hs$  show greater correlation with  $h$  from occupancy images since these measures depend on the same input data for classification. Regardless, there is not an apparent functional dependence for  $h$  with either measure.

The relationship between all measures and ice area fraction is depicted in Figure 4b. The  $q$ -statistic increases with area fraction although it demonstrates variability below area fractions of 0.3.  $Hs$  is highly variable for area fractions below 0.2 and decreasing afterward. The  $R^2$  values for these measures are 0.402 and 0.540 with  $p$ -values of 0.004 and  $3.4 \times 10^{-4}$ , respectively. Despite significant correlations, both parameters are inconsistent when applied to near-homogeneous images and report similar values for images with area fractions above 0.5. The heterogeneity index does not display a clear trend for grayscale images, producing an  $R^2$  of 0.475 and a  $p$ -value of 0.001. Initially  $h$  increases as the system becomes more heterogeneous with the inclusion of additional voids but as the ratio of open ocean begins to dominate,  $h$  decreases since the system becomes more homogeneous. Additionally, index values are small relative to other measures indicating the additional fidelity present in the grayscale images serves to reduce variance between scales in a similar manner to FBF systems.

Heterogeneity index values from occupancy images are linear with area fraction producing an  $R^2$  value of 0.967 and a  $p$ -value of  $5.0 \times 10^{-14}$ . Unlike the values obtained from grayscale images,  $h$  consistently increases with area fraction. This behavior can be explained by noting the ice occupancy images with large voids resemble Poisson point clusters. If the proportion of open ocean were increased further, this system would reduce to point clusters with proportionally higher index values. Therefore, in the context of characterizing sea ice structure, the proposed heterogeneity index provides a clear linear mapping.

While the proposed index is useful for identifying trends in spatial heterogeneity, it does not provide complete system characterization. By reducing lacunarity curves to a single value, information on significant length scales and fractal behavior are obscured. Although these features are an integral component of index assignment, it is not immediately apparent what spatial structures lead to a given index value beyond broad classifications. As such, we recommend incorporating the heterogeneity index into complimentary analyses where specialized techniques follow index assignment to determine the influence of relevant spatial structures. For instance, we noted large areas of continuous ice lead to lower index values while images with sparse ice distributions produce higher index values. Further analysis could assess the impact connectivity via contiguity indices for images with low index values, the fractal behavior of fracture networks through the multifractal spectra for images with midrange index values, the spatial distribution of melt pools via the  $q$ -statistic for images with midrange



values, and the clustering of pack ice for images with high index values. Many of the suggested studies have been performed and are listed as examples of how heterogeneity index assignment can inform secondary analyses.

#### 4. Conclusions

A measure for spatial heterogeneity based on lacunarity was proposed and the cutoff point required to encapsulate heterogeneity for a given system identified. The derivation of these quantities as well as a method to compute the required lacunarity values were detailed. The behavior of the cutoff function and heterogeneity index were documented in response to monofractal, clustered, and periodic systems. The heterogeneity index was found to describe both the proportion and distribution of mass in a system. Systems with fine detail produced higher heterogeneity assignments while smoothly varying systems struggled to develop a cutoff point and generated lower index values. Our approach was applied to sea ice images where the heterogeneity index based on binary ice occupancy images demonstrated a linear trend with area fraction and outperformed existing measures.

Because the heterogeneity index includes information from the full range of scales present in a system, it is well suited to quantifying multiscale phenomena. We anticipate our approach will benefit fields where spatial heterogeneity is a driving force behind observed phenomena by enabling the quantitative characterization of these systems.

#### Appendix A: Lacunarity Algorithm

Our approach for calculating lacunarity is built on the gliding box algorithm proposed by Allain and Cloitre (1991). In order to improve computation time, box translation is achieved through the dot product. For two-dimensional input data,  $\mathbf{A}$ , of size  $m \times n$  we define a box matrix,  $\mathbf{B}_1$ , as a  $k \times m$  rectangular diagonal matrix where  $k = m - r + 1$ . If  $r = 1$ ,  $\mathbf{B}_1$  reduces to the identity matrix and for larger values of  $r$ , takes the form of

$$\mathbf{B}_1 = \begin{bmatrix} 1_{1,1} & \dots & 1_{1,r} & & & \\ & 1_{2,2} & \dots & 1_{2,1+r} & & \\ & & \ddots & \ddots & \ddots & \\ & & & 1_{k,m-r} & \dots & 1_{k,m} \end{bmatrix} \quad (\text{A1})$$

The partial sum in one direction is calculated with

$$\mathbf{P} = \mathbf{B}_1 \cdot \mathbf{A} \quad (\text{A2})$$

Next, a new box matrix,  $\mathbf{B}_2$ , of size  $k \times n$  where  $k = n - r + 1$  is defined and the sum in the second direction is completed with

$$\mathbf{M} = \mathbf{B}_2 \cdot \mathbf{P}^T \quad (\text{A3})$$

Finally, the lacunarity value is calculated from  $\mathbf{M}$ . This process is repeated for each value of  $r$  to create the lacunarity curve.

The same approach is applicable to one-dimensional and three-dimensional input data. In one dimension, a single box matrix is sufficient and in three dimensions, an additional box matrix is required. Here, the input data must be restructured to create a two-dimensional matrix. When  $\mathbf{A}$  is of size  $m \times n \times l$ , every  $l$  plane of  $m \times n$  data is placed sequentially to create a matrix of size  $m \times n \cdot l$ . The box matrix for this transformation is of size  $k \times m$  where  $k = m - r + 1$ . To complete the sum in three directions, three such transformations are required to reframe the input data as  $n \times m \cdot l$  and  $l \times m \cdot n$  matrices.

Unlike prior algorithms, our approach is not limited to equidimensional systems. When a boundary is encountered,  $r$  continues to expand in the remaining unconstrained dimensions until reaching the full extent of the domain. However, irregular domains pose additional complications since  $r$  is no longer representative of a uniform sampling window. For example, if a system measured  $50 \times 300$  units and developed a cutoff point of  $r_a = 200$  units, the true sampling region would measure  $50 \times 200$  units. This limitation reduces the amount of

new information gained per sample which appears as a change in slope on the lacunarity curve each time a dimension is constrained. Consequently, equivalent systems with different domain sizes may develop identical cutoff points but will yield different heterogeneity index values. It is worth noting these limitations are not exclusive to lacunarity. As a consequence of their operation, box counting metrics in general as well as their derived indices are influenced by sample domain. Furthermore, domain size limitations are known to obscure the relationship between scales in naturally occurring systems (Serafino et al., 2021). Therefore, to conduct meaningful comparisons between systems, each domain should have an equivalent aspect ratio and range of  $r$ .

### Appendix B: Complete Solution for $\bar{R}_H$ and $h$

The complete procedure for determining the weighted average length scale for an equivalent homogeneous domain begins with the weighted average length scale defined in Equation 3 and written here for clarity

$$\bar{R}_w = \frac{1}{N_{\max}} \sum_{i=1}^{N_{\max}} \frac{r_i \Lambda(r_i)}{\Lambda(1)} \quad (\text{B1})$$

In the homogeneous case,  $\bar{R}_H$ , system variance is 0 and  $\Lambda(r) = 1$  for all values of  $r$  thus

$$\bar{R}_H = \frac{1}{N_{\max}} \sum_{i=1}^{N_{\max}} r_i \quad (\text{B2})$$

Evaluating the summation in terms of  $N_{\max}$  and recalling  $r(N_{\max}) = r_{\max}$  produces

$$\bar{R}_H = \frac{1}{N_{\max}} \left( \frac{N_{\max} (1 + r(N_{\max}))}{2} \right) = \frac{1 + r_{\max}}{2} \quad (\text{B3})$$

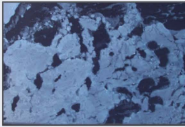
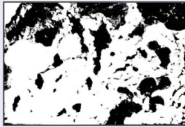
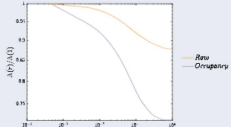
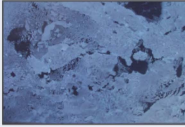
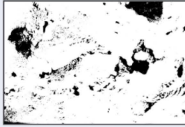
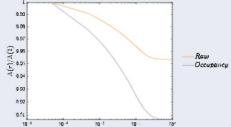
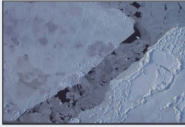

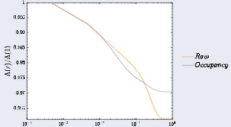
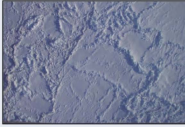

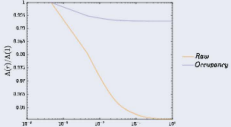
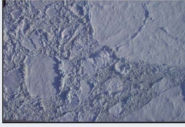
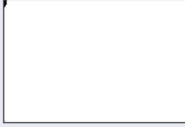
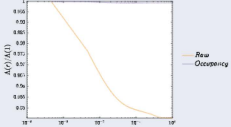


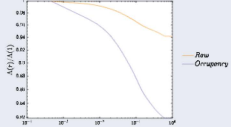

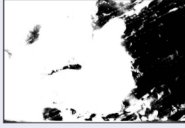
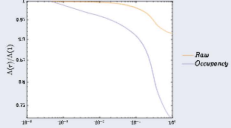
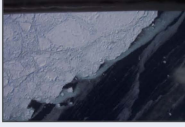
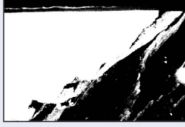
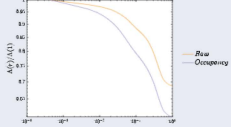
Subtracting Equation 1 from  $\bar{R}_H$  and rearranging yields the heterogeneity index

$$h = \frac{1 + r_{\max}}{2} - \bar{R}_H = 1 - \frac{2\bar{R}_w}{1 + r_{\max}} \quad (\text{B4})$$

### Appendix C: Sea Ice Results

Raw and processed sea ice images from the AMSRice06 Data Base including image reference identifier and index assignments. Each image pair is processed following the procedure outlined in Section 3.2 and shown alongside its respective lacunarity curves.

**Table C1**  
Complete Set of Selected Images From the AMSRice06 Data Base With Corresponding Cutoff and Index Values


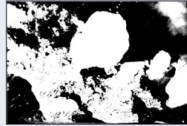
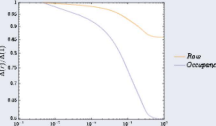

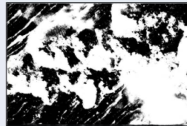
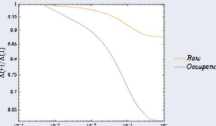
00681 DCP 6103 $r_{d,I} = 1.0, r_{a,B} = 0.90$ $h_I = 0.12, h_B = 0.28$ $q = 0.70, Hs = 0.75$			
00683 DCP 6104 $r_{a,I} = 0.67, r_{a,B} = 0.73$ $h_I = 0.05, h_B = 0.09$ $q = 0.54, Hs = 0.86$			
00717 DCP 6121 $r_{d,I} = 1.0, r_{a,B} = 0.88$ $h_I = 0.04, h_B = 0.03$ $q = 0.31, Hs = 1.06$			
01223 DCP 6330 $r_{a,I} = 0.71, r_{a,B} = 0.61$ $h_I = 0.04, h_B = 0.007$ $q = 0.03, Hs = 1.04$			
01225 DCP 6331 $r_{a,I} = 0.98, r_{a,B} = 0.50$ $h_I = 0.05, h_B = 0.001$ $q = 0.009, Hs = 1.45$			
01265 DCP 6351 $r_{d,I} = 1.0, r_{a,B} = 0.79$ $h_I = 0.06, h_B = 0.17$ $q = 0.62, Hs = 0.85$			
01580 DCP 6478 $r_{d,I} = 1.0, r_{d,B} = 1.0$ $h_I = 0.07, h_B = 0.25$ $q = 0.67, Hs = 0.80$			
01611 DCP 6693 $r_{d,I} = 1.0, r_{d,B} = 1.0$ $h_I = 0.28, h_B = 0.37$ $q = 0.70, Hs = 0.71$			

Note. Full resolution raw and ice occupancy images are available alongside the MATLAB codes used for analysis

Table C2. Continued From Table C1

<p>01790 DCP 6583  <math>r_{d,I} = 1.0, r_{d,B} = 1.0</math>  <math>h_I = 0.06, h_B = 0.06</math>  <math>q = 0.38, Hs = 0.93</math></p>			
<p>01792 DCP 6584  <math>r_{d,I} = 1.0, r_{a,B} = 0.62</math>  <math>h_I = 0.04, h_B = 0.05</math>  <math>q = 0.44, Hs = 0.89</math></p>			
<p>01796 DCP 6586  <math>r_{d,I} = 1.0, r_{a,B} = 0.62</math>  <math>h_I = 0.02, h_B = 0.02</math>  <math>q = 0.26, Hs = 1.08</math></p>			
<p>01798 DCP 6587  <math>r_{a,I} = 0.95, r_{d,B} = 1.0</math>  <math>h_I = 0.06, h_B = 0.15</math>  <math>q = 0.74, Hs = 0.91</math></p>			
<p>01800 DCP 6588  <math>r_{d,I} = 1.0, r_{d,B} = 1.0</math>  <math>h_I = 0.04, h_B = 0.09</math>  <math>q = 0.25, Hs = 0.87</math></p>			
<p>01802 DCP 6589  <math>r_{d,I} = 1.0, r_{a,B} = 0.88</math>  <math>h_I = 0.02, h_B = 0.01</math>  <math>q = 0.60, Hs = 0.83</math></p>			
<p>01834 DCP 6605  <math>r_{a,I} = 0.77, r_{d,B} = 1.0</math>  <math>h_I = 0.11, h_B = 0.20</math>  <math>q = 0.64, Hs = 0.72</math></p>			
<p>01836 DCP 6606  <math>r_{d,I} = 1.0, r_{a,B} = 0.93</math>  <math>h_I = 0.10, h_B = 0.34</math>  <math>q = 0.63, Hs = 0.72</math></p>			
<p>01838 DCP 6607  <math>r_{a,I} = 0.80, r_{a,B} = 0.90</math>  <math>h_I = 0.09, h_B = 0.48</math>  <math>q = 0.63, Hs = 0.70</math></p>			

Table C3. Continued From Table C1

01842 DCP 6609 $r_{a,I} = 0.97$ , $r_{a,B} = 0.78$ $h_I = 0.14$ , $h_B = 0.39$ $q = 0.70$ , $H_s = 0.70$			
01844 DCP 6610 $r_{d,I} = 1.0$ , $r_{d,B} = 1.0$ $h_I = 0.12$ , $h_B = 0.37$ $q = 0.65$ , $H_s = 0.71$			

### Data Availability Statement

Our lacunarity algorithm and all MATLAB code used to produce the results presented in this document are available at <https://zenodo.org/badge/latest/doi/350845334>. Full resolution raw and processed sea ice images are available alongside the MATLAB codes. Original sea ice images are from the AMSRice06 data set (Krabill, 2006) located at <https://cmr.earthdata.nasa.gov/search/concepts/C1386205191-NSIDCV0.html>.

### Acknowledgments

The authors would like to thank the Portland Institute for Computational Science and its resources acquired using National Science Foundation Grant DMS-1624776 for access to the Coeus HPC cluster. Raúl Bayoan Cal thanks the National Science Foundation Grant NSF-PDM-1712532. In addition, Marc Calaf thanks the support of the National Science Foundation Grants PDM-1649067, and PDM-1712538 as well as the support of the Alexander von Humboldt Stiftung/Foundation, Humboldt Research Fellowship for Experienced Researchers, during the sabbatical year at the Karlsruhe Institute of Technology Campus Alpin in Garmisch-Partenkirchen.

### References

- Allain, C., & Cloitre, M. (1991). Characterizing the lacunarity of random and deterministic fractal sets. *Physical Review A*, 44(6), 35–52. <https://doi.org/10.1103/physreva.44.3552>
- Allison, I., Brandt, R. E., & Warren, S. G. (1993). East Antarctic sea ice: Albedo, thickness distribution, and snow cover. *Journal of Geophysical Research*, 98(C7), 12417–12429. <https://doi.org/10.1029/93JC00648>
- Andreas, E., Paulson, C., William, R., Lindsay, R., & Businger, J. (1979). The turbulent heat flux from arctic leads. *Boundary-Layer Meteorology*, 17(1), 57–91. <https://doi.org/10.1007/bf00121937>
- Andreas, E. L. (1980). Estimation of heat and mass fluxes over arctic leads. *Monthly Weather Review*, 108(12), 2057–2063. [https://doi.org/10.1175/1520-0493\(1980\)108<2057:eoahmf>2.0.co;2](https://doi.org/10.1175/1520-0493(1980)108<2057:eoahmf>2.0.co;2)
- Andronache, I. C., Ahammer, H., Jelinek, H. F., Peptenatu, D., Ciobotaru, A.-M., Draghici, C. C., et al. (2016). Fractal analysis for studying the evolution of forests. *Chaos, Solitons & Fractals*, 91, 310–318. <https://doi.org/10.1016/j.chaos.2016.06.013>
- Backes, A. R. (2013). A new approach to estimate lacunarity of texture images. *Pattern Recognition Letters*, 34(13), 1455–1461. <https://doi.org/10.1016/j.patrec.2013.05.008>
- Borys, P., Krasowska, M., Grzywna, Z. J., Djamgoz, M. B., & Mycielska, M. E. (2008). Lacunarity as a novel measure of cancer cells behavior. *Biosystems*, 94(3), 276–281. <https://doi.org/10.1016/j.biosystems.2008.05.036>
- Claramunt, C. (2005). A spatial form of diversity. In *International Conference on Spatial Information Theory* (pp. 218–231). [https://doi.org/10.1007/11556114\\_14](https://doi.org/10.1007/11556114_14)
- Dougherty, G., & Henebry, G. M. (2001). Fractal signature and lacunarity in the measurement of the texture of trabecular bone in clinical CT images. *Medical Engineering & Physics*, 23(6), 369–380. [https://doi.org/10.1016/s1350-4533\(01\)00057-1](https://doi.org/10.1016/s1350-4533(01)00057-1)
- Drüe, C., & Heinemann, G. (2001). Airborne investigation of arctic boundary-layer fronts over the marginal ice zone of the Davis strait. *Boundary-Layer Meteorology*, 101(2), 261–292. <https://doi.org/10.1023/a:1019223513815>
- Du, G., & Yeo, T. S. (2002). A novel lacunarity estimation method applied to SAR image segmentation. *IEEE Transactions on Geoscience and Remote Sensing*, 40(12), 2687–2691. <https://doi.org/10.1109/tgrs.2002.1006395>
- Frazer, G. W., Wulder, M. A., & Niemann, K. O. (2005). Simulation and quantification of the fine-scale spatial pattern and heterogeneity of forest canopy structure: A lacunarity-based method designed for analysis of continuous canopy heights. *Forest Ecology and Management*, 214(1–3), 65–90. <https://doi.org/10.1016/j.foreco.2005.03.056>
- Gould, D. J., Vadakkan, T. J., Poché, R. A., & Dickinson, M. E. (2011). Multifractal and lacunarity analysis of microvascular morphology and remodeling. *Microcirculation*, 18(2), 136–151. <https://doi.org/10.1111/j.1549-8719.2010.00075.x>
- Hadjilontiadis, L. J. (2009). A texture-based classification of crackles and squawks using lacunarity. *IEEE Transactions on Biomedical Engineering*, 56(3), 718–732. <https://doi.org/10.1109/tbme.2008.2011747>
- Kirkpatrick, L. A., & Weishampel, J. F. (2005). Quantifying spatial structure of volumetric neutral models. *Ecological Modelling*, 186(3), 312–325. <https://doi.org/10.1016/j.ecolmodel.2005.01.056>
- Krabill, W. B. (2006). AMSRice06 aerial photographs. In *NASA DAAC at the National Snow and Ice Data Center*.
- Kroese, D. P., & Botev, Z. I. (2015). Spatial process simulation. In *Stochastic geometry, spatial statistics and random fields* (pp. 369–404). Springer. [https://doi.org/10.1007/978-3-319-10064-7\\_12](https://doi.org/10.1007/978-3-319-10064-7_12)
- Liu, K., & Ostad Hassan, M. (2017). Quantification of the microstructures of Bakken shale reservoirs using multi-fractal and lacunarity analysis. *Journal of Natural Gas Science and Engineering*, 39, 62–71. <https://doi.org/10.1016/j.jngse.2017.01.035>
- Malhi, Y., & Román-Cuesta, R. M. (2008). Analysis of lacunarity and scales of spatial homogeneity in Ikonos images of Amazonian tropical forest canopies. *Remote Sensing of Environment*, 112(5), 2074–2087. <https://doi.org/10.1016/j.rse.2008.01.009>
- Mandelbrot, B. B. (1982). *The fractal geometry of nature* (Vol. 2). New York: WH Freeman.
- Payne, R. E. (1972). Albedo of the sea surface. *Journal of the Atmospheric Sciences*, 29(5), 959–970. [https://doi.org/10.1175/1520-0469\(1972\)029<0959:aooss>2.0.co;2](https://doi.org/10.1175/1520-0469(1972)029<0959:aooss>2.0.co;2)

- Perovich, D. K., & Polashenski, C. (2012). Albedo evolution of seasonal arctic sea ice. *Geophysical Research Letters*, 39, L08501. <https://doi.org/10.1029/2012GL051432>
- Plotnick, R. E., Gardner, R. H., Hargrove, W. W., Prestegard, K., & Perlmutter, M. (1996). Lacunarity analysis: A general technique for the analysis of spatial patterns. *Physical Review E*, 53(5), 5461. <https://doi.org/10.1103/physreve.53.5461>
- Plotnick, R. E., Gardner, R. H., & O'Neill, R. V. (1993). Lacunarity indices as measures of landscape texture. *Landscape Ecology*, 8(3), 201–211. <https://doi.org/10.1007/bf00125351>
- Popovic, N., Radunovic, M., Badnjar, J., & Popovic, T. (2018). Fractal dimension and lacunarity analysis of retinal microvascular morphology in hypertension and diabetes. *Microvascular Research*, 118, 36–43. <https://doi.org/10.1016/j.mvr.2018.02.006>
- Reiss, M. A., Lemmerer, B., Hanslmeier, A., & Ahammer, H. (2016). Tug-of-war lacunarity—A novel approach for estimating lacunarity. *Chaos: An Interdisciplinary Journal of Nonlinear Science*, 26(11), 113102. <https://doi.org/10.1063/1.4966539>
- Saunders, S. C., Chen, J., Drummer, T. D., Gustafson, E. J., & Brososke, K. D. (2005). Identifying scales of pattern in ecological data: A comparison of lacunarity, spectral and wavelet analyses. *Ecological Complexity*, 2(1), 87–105. <https://doi.org/10.1016/j.ecocom.2004.11.002>
- Sengupta, K., & Vinoy, K. (2006). A new measure of lacunarity for generalized fractals and its impact in the electromagnetic behavior of Koch dipole antennas. *Fractals*, 14(4), 271–282. <https://doi.org/10.1142/s0218348x06003313>
- Serafino, M., Cimini, G., Maritan, A., Rinaldo, A., Suweis, S., Banavar, J. R., & Caldarelli, G. (2021). True scale-free networks hidden by finite size effects. *Proceedings of the National Academy of Sciences of the United States of America*, 118(2), e2013825118. <https://doi.org/10.1073/pnas.2013825118>
- Shaw, W. J., Pauley, R. L., Gobel, T. M., & Radke, L. F. (1991). A case study of atmospheric boundary layer mean structure for flow parallel to the ice edge: Aircraft observations from CEAREX. *Journal of Geophysical Research*, 96(C3), 4691–4708. <https://doi.org/10.1029/90JC01953>
- Sierpiński, W. (1916). Sur une courbe cantorienne qui contient une image biunivoque et continue de toute courbe donnée. *Comptes rendus de l'Académie des Sciences*, 162, 629–632.
- Tetzlaff, A., Lüpkes, C., & Hartmann, J. (2015). Aircraft-based observations of atmospheric boundary-layer modification over arctic leads. *Quarterly Journal of the Royal Meteorological Society*, 141(692), 2839–2856. <https://doi.org/10.1002/qj.2568>
- Tolle, C. R., McJunkin, T. R., & Gorsich, D. J. (2008). An efficient implementation of the gliding box lacunarity algorithm. *Physica D: Nonlinear Phenomena*, 237(3), 306–315. <https://doi.org/10.1016/j.physd.2007.09.017>
- Wang, J.-F., Zhang, T.-L., & Fu, B.-J. (2016). A measure of spatial stratified heterogeneity. *Ecological Indicators*, 67, 250–256. <https://doi.org/10.1016/j.ecolind.2016.02.052>
- Williams, D. P. (2015). Fast unsupervised seafloor characterization in sonar imagery using lacunarity. *IEEE Transactions on Geoscience and Remote Sensing*, 53(11), 6022–6034. <https://doi.org/10.1109/tgrs.2015.2431322>
- With, K. A., & King, A. W. (1999). Dispersal success on fractal landscapes: A consequence of lacunarity thresholds. *Landscape Ecology*, 14(1), 73–82. <https://doi.org/10.1023/a:1008030215600>
- Xia, Y., Cai, J., Perfect, E., Wei, W., Zhang, Q., & Meng, Q. (2019). Fractal dimension, lacunarity and succolarity analyses on CT images of reservoir rocks for permeability prediction. *Journal of Hydrology*, 579, 124–198. <https://doi.org/10.1016/j.jhydrol.2019.124198>
- Yasar, F., & Akgunlu, F. (2005). Fractal dimension and lacunarity analysis of dental radiographs. *Dentomaxillofacial Radiology*, 34(5), 261–267.
- Zeng, Y., Payton, R., Gantzer, C., & Anderson, S. H. (1996). Fractal dimension and lacunarity of bulk density determined with X-ray computed tomography. *Soil Science Society of America Journal*, 60(6), 1718–1724. <https://doi.org/10.2136/sssaj1996.03615995006000060016x>